

Research Paper

A Biomimetic Gold Nanocages-Based NanoplatforM for Efficient Tumor Ablation and Reduced Inflammation

Qingbo Xu¹, Jiangshan Wan¹, Nana Bie¹, Xianlin Song², Xiaoquan Yang², Tuying Yong¹, Yanbing Zhao¹, Xiangliang Yang¹✉, Lu Gan¹✉

1. National Engineering Research Center for Nanomedicine, Hubei Key Laboratory of Bioinorganic Chemistry and Materia Medica, College of Life Science and Technology, Huazhong University of Science and Technology, Wuhan 430074, China
2. Britton Chance Center for Biomedical Photonics, Wuhan National Laboratory for Optoelectronics & Moe Key Laboratory of Biomedical Photonics of Ministry of Education, Department of Biomedical Engineering, Huazhong University of Science and Technology, Wuhan 430074, China

✉ Corresponding authors: E-mail: lugan@mail.hust.edu.cn (L. Gan) Or yangxl@mail.hust.edu.cn (X. Yang)

© Ivyspring International Publisher. This is an open access article distributed under the terms of the Creative Commons Attribution (CC BY-NC) license (<https://creativecommons.org/licenses/by-nc/4.0/>). See <http://ivyspring.com/terms> for full terms and conditions.

Received: 2018.06.03; Accepted: 2018.10.04; Published: 2018.10.24

Abstract

Gold nanocages (AuNCs), with high photothermal conversion efficiency and unique hollow interiors, have become a promising nanoplatforM for synergistic phototheraml therapy (PTT)-chemotherapy. However, the insufficient tumor targeting, in vivo premature drug leakage and low drug loading efficiency responsible for the spatial-temporal un-synchronization of PTT-chemotherapy, as well as inflammatory response might compromise the anticancer treatment of AuNCs-based drug delivery systems.

Methods: Cancer cell membrane (CCM)-coated AuNCs were developed to load anticancer drug doxorubicin (DOX@CAuNCs) by transmembrane ammonium sulfate gradient method. In vitro and in vivo analysis, including characterization, macrophage phagocytosis and tumor targeting capacity, near-infrared (NIR) laser-induced drug release, antitumor efficacy and inflammation response were systematically performed.

Results: DOX@CAuNCs showed a high DOX loading capacity and on-demand NIR laser-triggered DOX release compared with CAuNCs passively loading DOX by electrostatic adsorption, a commonly used method to load drug to AuNCs. Meanwhile, in view of the properties of CCM coated on AuNCs, DOX@CAuNCs exhibited decreased macrophage phagocytosis, prolonged blood circulation and enhanced internalization by cancer cells, generating preferable tumor targeting ability. With these integrated advantages, DOX@CAuNCs demonstrated highly efficient and precise spatial-temporal synchronization of PTT-chemotherapy, achieving complete tumor ablation with no obvious side effects. Besides, coating with CCM significantly alleviated AuNCs-induced inflammatory response.

Conclusion: This biomimetic AuNCs-based platform might be a prospective drug delivery system for precision PTT and chemotherapy, acquiring desired cancer treatment efficacy and low inflammatory response.

Key words: Gold nanocages, cancer cell membrane, high drug loading efficiency, spatial-temporal synchronization of photothermal-chemotherapy, inflammation, cancer therapy

Introduction

Near-infrared (NIR) laser-triggered photothermal therapy (PTT) has been widely recognized as a promising strategy for cancer treatment owing to its minimal invasiveness and deep

tissue penetration capacity [1,2]. However, the uneven heat distribution within tumor regions and gradual reduction in laser intensity as it travels through tumor parenchyma might result in the incomplete irradiation

of tumor cells, especially those located in deep tumor region [3,4]. Considering that PTT not only enhances the sensitivity of cancer cells to chemotherapy [5,6], but also increases blood flow to the heated area and augments tumor vascular permeability to promote the delivery of chemotherapeutic drug to deep tumor tissues [7], the development of spatial-temporal synchronization of PTT-chemotherapy is highly desirable for efficient cancer treatment with synergistic effect [8,9].

Nanoparticles have the extraordinary capacity to combine different treatment strategies into a synergetic platform for cancer therapy [10-13]. Gold nanocages (AuNCs), with tunable localized surface plasmon resonance (LSPR) peaks in the NIR region and high photothermal conversion efficiency, have been actively used as photothermal conversion agents for PTT [14]. Simultaneously, the unique hollow interiors and porous well structure of AuNCs confer them potential to load anticancer drug [15], which makes them particularly attractive for synergistic PTT-chemotherapy. However, insufficient tumor targeting, *in vivo* premature drug leakage due to their open pore outlets [16], and inflammatory response [17], restrict their therapeutic efficacy. Nowadays, several strategies have been used to solve these issues. For example, functionalization of AuNCs with a ligand that binds to a receptor overexpressed on cancer cells was used to enhance their targeting to tumor site [18,19]. AuNCs were modified with thermally responsive polymers and calcium phosphate-coated nanoparticles to block pore outlets to evade premature drug release in blood circulation, while the loaded drug can be released at the tumor site in a controllable fashion using various stimuli, including NIR laser irradiation [20], high-intensity focused ultrasound [21,22], and pH [23]. However, the drug was usually incorporated into AuNCs by electrostatic adsorption, resulting in the low drug loading efficiency and the release of the vast majority of drug by single irradiation [15,23], which might generate only PTT in subsequent irradiation and unsatisfactory therapeutic outcome. Therefore, it still remains a big challenge to develop AuNCs-based drug delivery system with high loading efficiency to achieve precise spatial-temporal synchronization of PTT-chemotherapy.

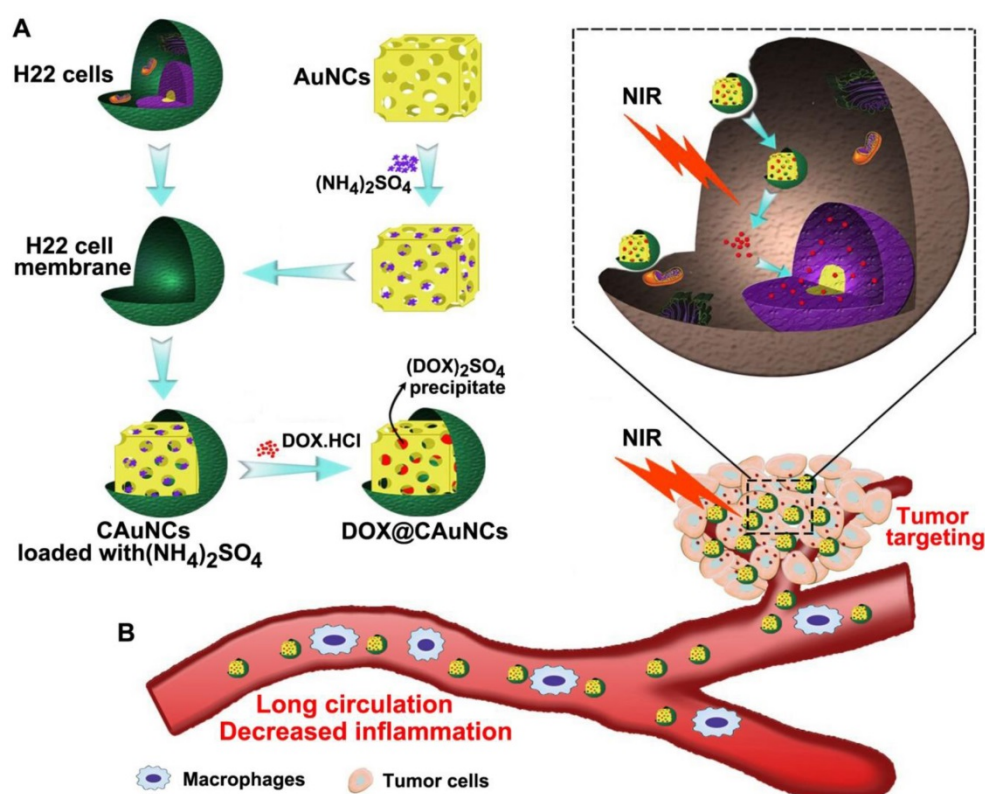
The biomimetic cancer cell membrane (CCM)-based nanoparticles have recently attracted considerable attentions as effective drug delivery platforms [24-26]. They have displayed good biocompatibility, prolonged circulation, favorable stability to decrease the leak of drugs in blood circulation, as well as excellent tumor-targeting capacity. Here, we develop CCM-coated AuNCs

(CAuNCs) to load anticancer drug doxorubicin (DOX) with high drug loading efficiency by transmembrane ammonium sulfate gradient method. At first, ammonium sulfate is loaded into AuNCs and then coated with CCM derived from murine hepatocarcinoma H22 cells. After incubation with DOX, DOX is driven into ammonium sulfate-loaded CAuNCs by virtue of base exchange of the amphipathic weak base of DOX with the ammonium ions (**Scheme 1A**). The CAuNCs loading DOX (DOX@CAuNCs) exhibit precisely on-demand drug release upon NIR laser irradiation at tumor sites, achieving the spatial-temporal synchronization of PTT-chemotherapy compared with CAuNCs loading DOX by electrostatic adsorption. Meanwhile, DOX@CAuNCs exhibit increased macrophage escape, prolonged circulation and good stability in blood, as well as enhanced tumor uptake. With these integrated advantages, DOX@CAuNCs cause highly efficient tumor ablation with no obvious side effects. In addition, CCM coating significantly decreases AuNCs-induced inflammatory response (**Scheme 1B**).

Results and Discussion

Preparation and Characterization of DOX@CAuNCs

In this work, AuNCs were first synthesized *via* a simple galvanic replacement reaction between Ag nanocubes and H₂AuCl₄ in an aqueous solution [27]. AuNCs were loaded with ammonium sulfate and then physically extruded with CCM from murine hepatocellular carcinoma H22 cells through a 200 nm porous polycarbonate membrane to obtain CAuNCs loaded with ammonium sulfate. Finally, DOX@CAuNCs were constructed by actively encapsulating DOX into CAuNCs by transmembrane ammonium sulfate gradient method. DOX loading capacity of DOX@CAuNCs could be easily modulated by changing the initial DOX input. The DOX loading capacity achieved 8.1% at the DOX/AuNCs feeding ratio of 1 (w/w), while it increased up to 55% at the DOX/AuNCs feeding ratio of 10 (w/w) (**Figure 1A**). In contrast, when DOX was passively loaded into CAuNCs (DOX_{passive}@CAuNCs), in which DOX was loaded into AuNCs through electrostatic adsorption and then the complex was encapsulated into CCM by physical extrusion, the DOX loading capacity only reached 4.4% even by increasing DOX input. Therefore, this active DOX loading by transmembrane ammonium sulfate gradient method could provide high and adjustable drug loading capacity as needed. The high drug loading efficiency of DOX@CAuNCs by transmembrane ammonium sulfate gradient method



Scheme 1. Schematic illustration of DOX@CAuNCs for precisely synergistic PTT-chemotherapy in cancer treatment. **(A)** Schematic illustration of the preparation of DOX@CAuNCs. **(B)** Schematic illustration of DOX@CAuNCs for long circulation, decreased inflammation, tumor targeting, NIR laser-triggered on demand drug release and precisely synergistic PTT-chemotherapy.

might be due to the existence of DOX in the form of $(\text{DOX})_2\text{SO}_4$ crystals in CAuNCs through base exchange of the amphipathic weak base of DOX with the ammonium ions [28,29]. In contrast, the weak electrostatic interaction between AuNCs and DOX in $\text{DOX}_{\text{passive}}\text{@CAuNCs}$ resulted in the low drug loading efficiency. Therefore, we used active transmembrane ammonium sulfate gradient method to load DOX to CAuNCs in the following experiments.

The hydrodynamic diameter and surface charge of AuNCs, CAuNCs and DOX@CAuNCs were determined by dynamic light scattering (DLS) (Figure 1B-C). After CCM coating, the hydrodynamic diameter of CAuNCs increased from 82.3 nm to 104.5 nm, while the surface charge shifted from -19.7 mV to -30.5 mV, almost similar to that of CCM. The change of hydrodynamic diameter and zeta potential of AuNCs before and after CCM coating revealed that AuNCs might be coated with CCM. DOX loading did not significantly change the hydrodynamic diameter and zeta potential of CAuNCs. Furthermore, UV-Vis-NIR spectra analysis showed that the LSPR peak position of AuNCs, CAuNCs and DOX@CAuNCs at about 800 nm was not changed. However, two new absorption peaks at about 220 and

260 nm obviously appeared in CCM, CAuNCs and DOX@CAuNCs (Figure 1D), further indicating the successful coating of CCM on AuNCs. Besides, transmission electron microscopy (TEM) images clearly demonstrated that a slight gray shell with a thickness of about 9 nm, which was in agreement with the reported cell membrane thickness [25], was coated on cube shaped-AuNCs in CAuNCs and DOX@CAuNCs (Figure 1E). Overall, these data strongly revealed that CAuNCs and DOX@CAuNCs were successfully fabricated.

The capacity of immune escape and targeting to cancer cells of CCM was reported

to be due to the antigens on the cell membrane [30]. To determine the maintenance of membrane proteins after coating on AuNCs, gel electrophoresis was first performed and then stained by Coomassie brilliant blue. As indicated in Figure 1F, the protein profiles of CAuNCs and DOX@CAuNCs coincided with that of the purified CCM, suggesting a good retention of membrane proteins after coating on AuNCs. Moreover, western blotting was performed to verify the presence of functional membrane proteins (Figure 1G). CD47 functions as a marker of “self” protein that impedes phagocytosis of self by signaling through phagocyte receptor CD172a [31,32]. CD54 (also referred as intercellular adhesion molecule, ICAM-1) mediates cell adhesion by binding to integrins CD11a/CD18 and CD11b/CD18 [33]. Consistently, similar to whole cell lysates and cell membrane lysates, CD47 and CD54 were also expressed in CAuNCs and DOX@CAuNCs. In contrast, β -actin, an intracellular protein, was merely found in cell lysates, but not in CCM, CAuNCs and DOX@CAuNCs. These results indicated that intracellular proteins were removed and membrane proteins were selectively reserved during the fabrication processing.

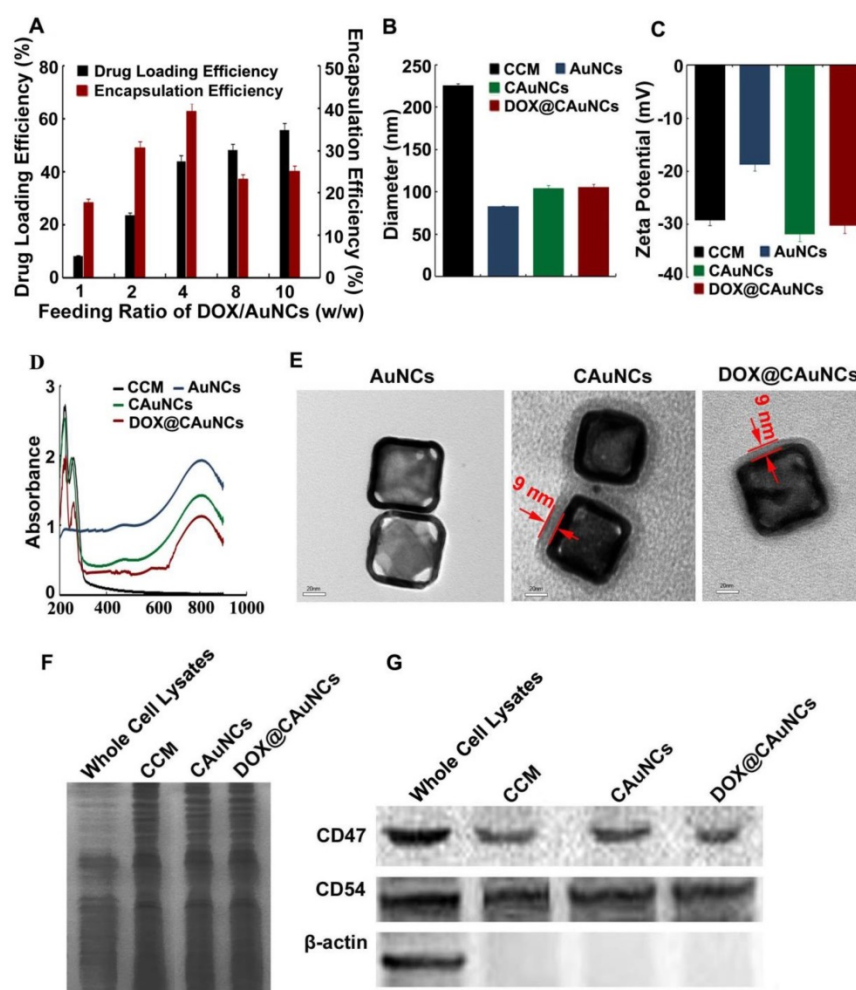


Figure 1. Characterization of DOX@CAuNCs. **(A)** Drug loading and encapsulation efficiency of DOX@CAuNCs when changing the feeding ratio of DOX and AuNCs by transmembrane ammonium sulfate gradient method. **(B)** Hydrodynamic diameter of CCM, AuNCs, CAuNCs and DOX@CAuNCs by DLS. **(C)** Zeta potential of CCM, AuNCs, CAuNCs and DOX@CAuNCs by DLS. Data as mean value \pm SD ($n=3$). **(D)** UV-vis-NIR absorption spectra of CCM, AuNCs, CAuNCs and DOX@CAuNCs. **(E)** TEM images of AuNCs, CAuNCs and DOX@CAuNCs. Scale bar: 20 nm. **(F)** Protein profiles of H22 cell lysates, H22 CCM, CAuNCs and DOX@CAuNCs by SDS-PAGE. **(G)** Western blotting analysis of membrane-specific protein markers (including CD47 and CD54) and intracellular protein marker β -actin in H22 cell lysates, H22 CCM, CAuNCs and DOX@CAuNCs.

In Vitro Photothermal Effects and on-Demand NIR Laser-Induced Drug Release of DOX@CAuNCs

As expected, AuNCs exhibited concentration- and laser power-dependent photothermal effects (Figure S1). To examine whether AuNCs retained photothermal effects after CCM coating and DOX loading, AuNCs, CAuNCs and DOX@CAuNCs dispersions were irradiated with 808 nm laser (1 W/cm^2) and the temperature of these aqueous solutions was determined (Figure 2A). AuNCs, CAuNCs and DOX@CAuNCs displayed similar temperature rise profiles and their temperature could quickly increase by 31.4°C after irradiation for 10 min. However, the temperature of PBS, CCM and DOX merely increased by 5.2°C after irradiation by 808 nm laser. These results demonstrated that CCM coating and DOX loading did not affect the photothermal effects of AuNCs. Furthermore, the

temperature rise profiles of AuNCs, CAuNCs and DOX@CAuNCs after NIR laser irradiation did not change even undergoing four irradiation-cooling cycles (Figure 2B), confirming their excellent photothermal stability. To determine NIR laser-controlled photothermal drug release from DOX@CAuNCs, the CCM integrity of DOX@CAuNCs in response to NIR laser irradiation was first evaluated. The gray shell coated on AuNCs was destroyed after NIR laser irradiation (Figure S2), suggesting that NIR laser-induced photothermal damage of CCM might contribute to DOX release from DOX@CAuNCs. Furthermore, the *in vitro* DOX release kinetics from DOX@CAuNCs was performed in PBS with or without NIR laser irradiation. As expected, only 16.1% DOX was released within 10 h at 37°C (Figure 2C), and the cumulative DOX release from DOX@CAuNCs was about 20.8% even within 72 h in the absence of NIR laser irradiation (Figure S3),

suggesting that DOX@CAuNCs were stable under physiological condition. However, DOX release from DOX@CAuNCs was accelerated upon 808 nm laser irradiation (Figure 2C). The cumulative DOX release increased from 8.5% to 17.1% upon 5 min NIR laser irradiation at 4 h. The same phenomenon with a rapid drug release upon NIR laser irradiation was observed in other cycles, and the cumulative DOX release reached up to 78.1% after seven cycles of 5 min irradiation at the designated time intervals within 10 h, suggesting the on-demand drug release from DOX@CAuNCs under NIR laser irradiation. The slow drug release of DOX@CAuNCs under physiological condition might be due to the existence of DOX in crystalline (DOX)₂SO₄ salt when using ammonium sulfate gradient method to load DOX. NIR laser-induced photothermal effects accelerated DOX release from DOX@CAuNCs on demand, which might generate precise synergy of PTT-chemotherapy. In contrast, the DOX release from DOX_{passive}@CAuNCs constructed by passive drug loading method reached 35.7 % within 24 h and 48.5 % within 72 h at 37 °C (Figure S3). DOX release rate increased by 69.3% upon one cycle of NIR laser irradiation, and almost all DOX was released after two cycles of NIR laser irradiation (Figure S4). The results suggested that DOX_{passive}@CAuNCs were not stable under physiological condition, which might be due to the weak electrostatic adsorption between AuNCs and DOX. Meanwhile, the weak electrostatic interaction between AuNCs and DOX resulted in the quick DOX release upon NIR laser irradiation and the un-synchronization of PTT-chemotherapy, which might affect the anticancer therapeutic effects.

Macrophage Escape and Long Circulation of DOX@CAuNCs

To investigate the macrophage escape capability

of DOX@CAuNCs, the interaction of AuNCs, CAuNCs or DOX@CAuNCs with fetal bovine serum (FBS) was first investigated (Figure S5A). CAuNCs and DOX@CAuNCs showed significantly decreased protein adsorption compared with AuNCs. Furthermore, mouse macrophage RAW264.7 cells were incubated with AuNCs, CAuNCs or DOX@CAuNCs in the presence or absence of FBS for various time intervals and then intracellular Au content was determined by inductively coupled plasma optical emission spectroscopy (ICP-OES) (Figure 3A and Figure S5B). The phagocytosis of AuNCs, CAuNCs and DOX@CAuNCs by macrophages increased in a time-dependent manner. However, the intracellular Au content in AuNCs-treated group was significantly higher than that in CAuNCs- and DOX@CAuNCs-treated groups both in the presence or absence of FBS, suggesting the excellent immune evasion ability of CAuNCs and DOX@CAuNCs. Furthermore, the *in vivo* pharmacokinetics was performed in SD rats intravenously injected with AuNCs, CAuNCs or DOX@CAuNCs. At different time points after injection, blood was collected and Au content was quantified using ICP-OES (Figure 3B and Table S1). Significantly enhanced blood retention was consistently observed in CAuNCs- and DOX@CAuNCs-treated groups as compared to AuNCs-treated group. The area under the curve (AUC) of both CAuNCs and DOX@CAuNCs was about 2.1-fold greater than that of AuNCs. In the meanwhile, the terminal elimination half-life ($t_{1/2\beta}$) of CAuNCs and DOX@CAuNCs was about 1.8- and 1.7-fold more than that of AuNCs. These results confirmed that coating of CCM might reduce the phagocytosis of AuNCs by reticuloendothelial system (RES), resulting in prolonged blood circulation.

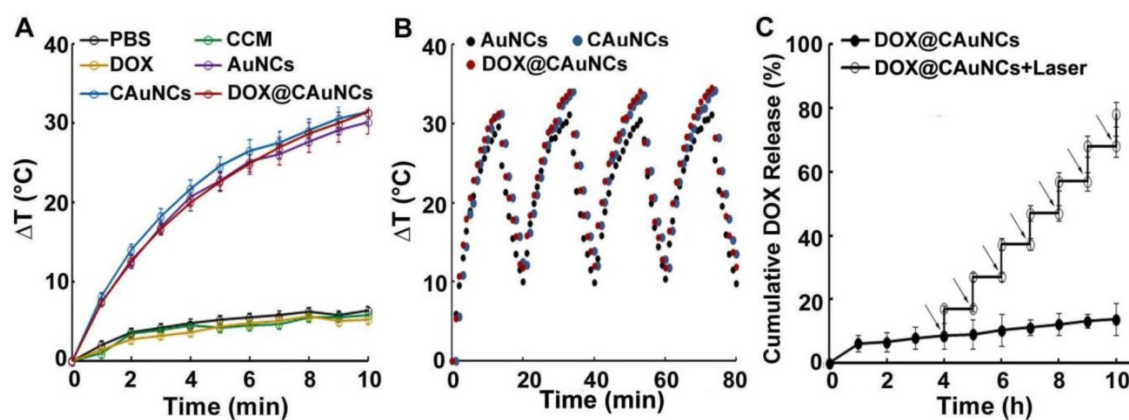


Figure 2. NIR laser-controlled photothermal drug release from DOX@CAuNCs. (A) Temperature change of PBS, CCM, DOX, AuNCs, CAuNCs and DOX@CAuNCs upon 808 nm laser irradiation (1 W/cm²) for different time intervals. (B) Photothermal stability of AuNCs, CAuNCs and DOX@CAuNCs in PBS subjected to four cycles of 808 nm laser irradiation (1 W/cm²) and then cooling at room temperature. (C) *In vitro* DOX release kinetics from DOX@CAuNCs in PBS at pH 7.4 in the presence or absence of 808 nm laser irradiation (1 W/cm²) for 5 min. Black arrows indicate the irradiation points. Data as mean value \pm SD (n=3).

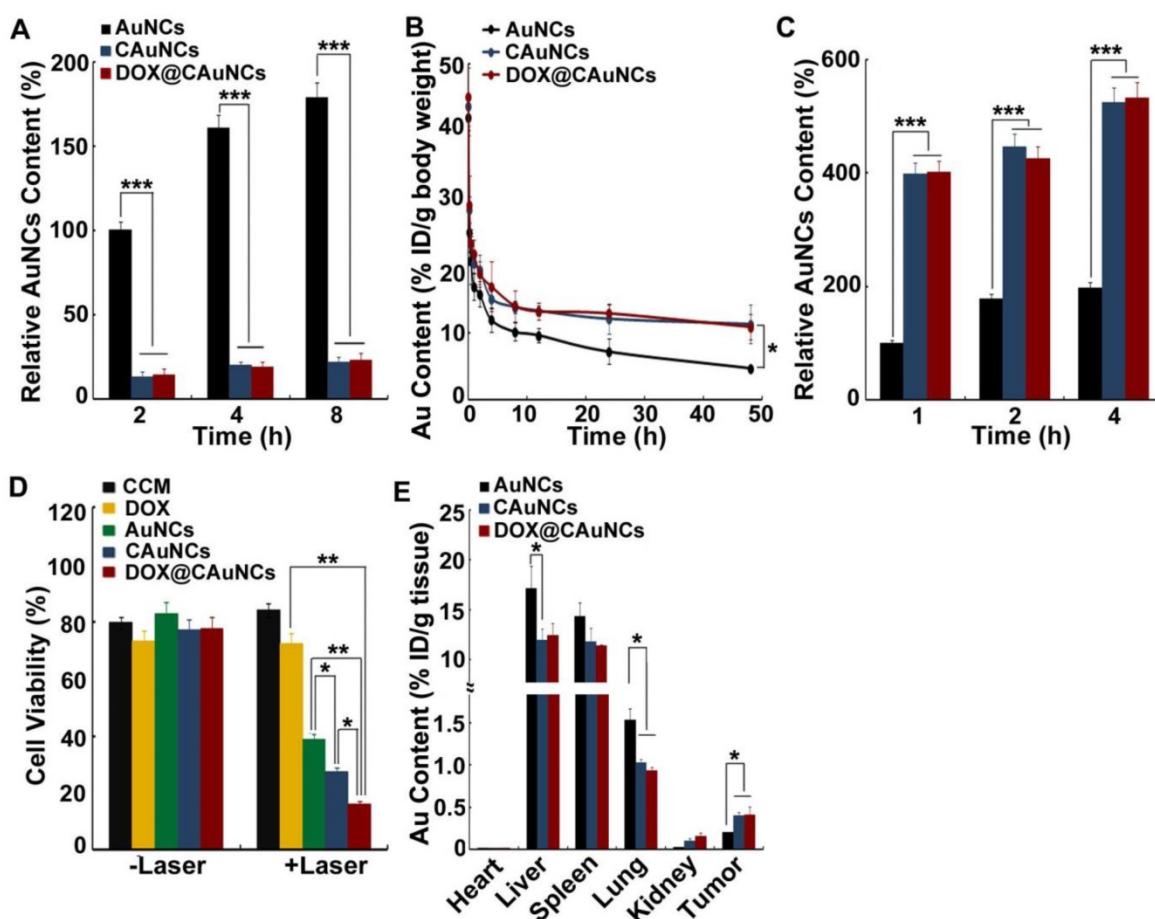


Figure 3. Long circulation and tumor targeting of DOX@CAuNCs. (A) Intracellular Au contents in RAW264.7 cells treated with AuNCs, CAuNCs or DOX@CAuNCs at Au concentration of 10 $\mu\text{g}/\text{mL}$ in the absence of FBS for different time intervals. (B) *In vivo* pharmacokinetics in SD rats after intravenous injection with AuNCs, CAuNCs or DOX@CAuNCs at Au dose of 10 mg/kg. (C) Intracellular Au contents in H22 cells treated with AuNCs, CAuNCs or DOX@CAuNCs at Au concentration of 10 $\mu\text{g}/\text{mL}$ in the absence of FBS for different time intervals. (D) Cell viability of H22 cells treated with CCM, DOX, AuNCs, CAuNCs or DOX@CAuNCs at Au and DOX concentration of 10 and 1.5 $\mu\text{g}/\text{mL}$ for 12 h, correspondingly, followed by 808 nm laser irradiation (1 W/cm²) for 5 min and then incubation in fresh medium for 8 h. (E) *In vivo* biodistribution of AuNCs, CAuNCs or DOX@CAuNCs in H22 tumor-bearing mice at 48 h after intravenous injection at Au dose of 10 mg/kg. Data as mean value \pm SD (n=4). * $P < 0.05$, ** $P < 0.01$, *** $P < 0.001$.

Cancer Cell Targeting and *in Vitro* Synergistic PTT-Chemotherapy of DOX@CAuNCs

It has been reported that CCM coating could enhance the cellular uptake of nanoparticles by cancer cells due to overexpression of some special surface antigens [32,34]. To determine the active cancer cell targeting capacity, H22 cells were incubated with AuNCs, CAuNCs or DOX@CAuNCs in the presence or absence of FBS for various time intervals and the intracellular Au contents were then quantified by ICP-OES (Figure 3C and Figure S5C). Intracellular Au contents increased in a time-dependent manner in H22 cells treated with AuNCs, CAuNCs or DOX@CAuNCs. CAuNCs and DOX@CAuNCs exhibited the higher intracellular accumulation than AuNCs in H22 cells. However, no significant difference was detected in the cellular uptake of AuNCs, CAuNCs and DOX@CAuNCs by normal NIH3T3 fibroblasts (Figure S6). These results demonstrated that CAuNCs and DOX@CAuNCs

exhibited the excellent cellular uptake by cancer cells. Furthermore, the endocytic pathway of DOX@CAuNCs was investigated in H22 cells (Figure S7). DOX@CAuNCs were internalized into H22 cells through an energy-dependent endocytosis. Meanwhile, 5-(*N*-ethyl-*N*-isopropyl) amiloride (EIPA, an inhibitor of macropinocytosis), chlorpromazine (CPZ, an inhibitor of clathrin-mediated endocytosis) and methyl- β -cyclodextrin (M β CD, an inhibitor of lipid raft/caveolae-mediated endocytosis) significantly inhibited the internalization of DOX@CAuNCs, suggesting that macropinocytosis-, clathrin- and lipid raft/caveolae-mediated endocytosis was involved in the internalization of DOX@CAuNCs. Moreover, the biological function of enhanced internalization of DOX@CAuNCs into cancer cells was evaluated. H22 cells were incubated with CCM, DOX, AuNCs, CAuNCs or DOX@CAuNCs for 12 h and then irradiated with or without 808 nm laser (1 W/cm²) for 5 min. After

another 8 h incubation, the cell cytotoxicity was evaluated using Cell counting kit-8 (CCK-8) assay (Figure 3D). Without NIR laser irradiation, no obvious cytotoxicity against H22 cells was detected in all groups. As expected, NIR laser irradiation-induced photothermal effects of AuNCs displayed strong cytotoxicity. However, CCM coating further enhanced the cytotoxicity induced by photothermal effects of AuNCs, which might be due to the enhanced internalization into cancer cells. The strongest cytotoxicity was detected in DOX@CAuNCs-treated group upon NIR laser irradiation, confirming the synergistic PTT-chemotherapy therapy.

To further explore the tumor targeting capacity of DOX@CAuNCs, the *in vivo* biodistribution was determined in H22 tumor-bearing mice intravenously injected with AuNCs, CAuNCs or DOX@CAuNCs. At 48 h after injection, the mice were sacrificed, and their

major organs (including heart, liver, spleen, lung and kidney) and tumors were collected for Au quantification by using ICP-OES. As shown in Figure 3E, more AuNCs were accumulated in liver and lung, which are regarded as phagocyte-enriched RES organs compared with CAuNCs and DOX@CAuNCs, confirming that CCM coating could decrease RES phagocytosis of AuNCs (Figure 3A) and prolong blood circulation of CAuNCs and DOX@CAuNCs (Figure 3B). In contrast, CAuNCs and DOX@CAuNCs were accumulated in tumors considerably higher than AuNCs, about 1.9- and 2.0-times more than AuNCs (Figure 3E), revealing that CAuNCs and DOX@CAuNCs exhibited excellent homologous tumor targeting ability. CCM coating-induced excellent tumor targeting capacity might result from the prolonged blood circulation contributing to their accumulation in tumor tissues by EPR effects and the enhanced cancer cell targeting.

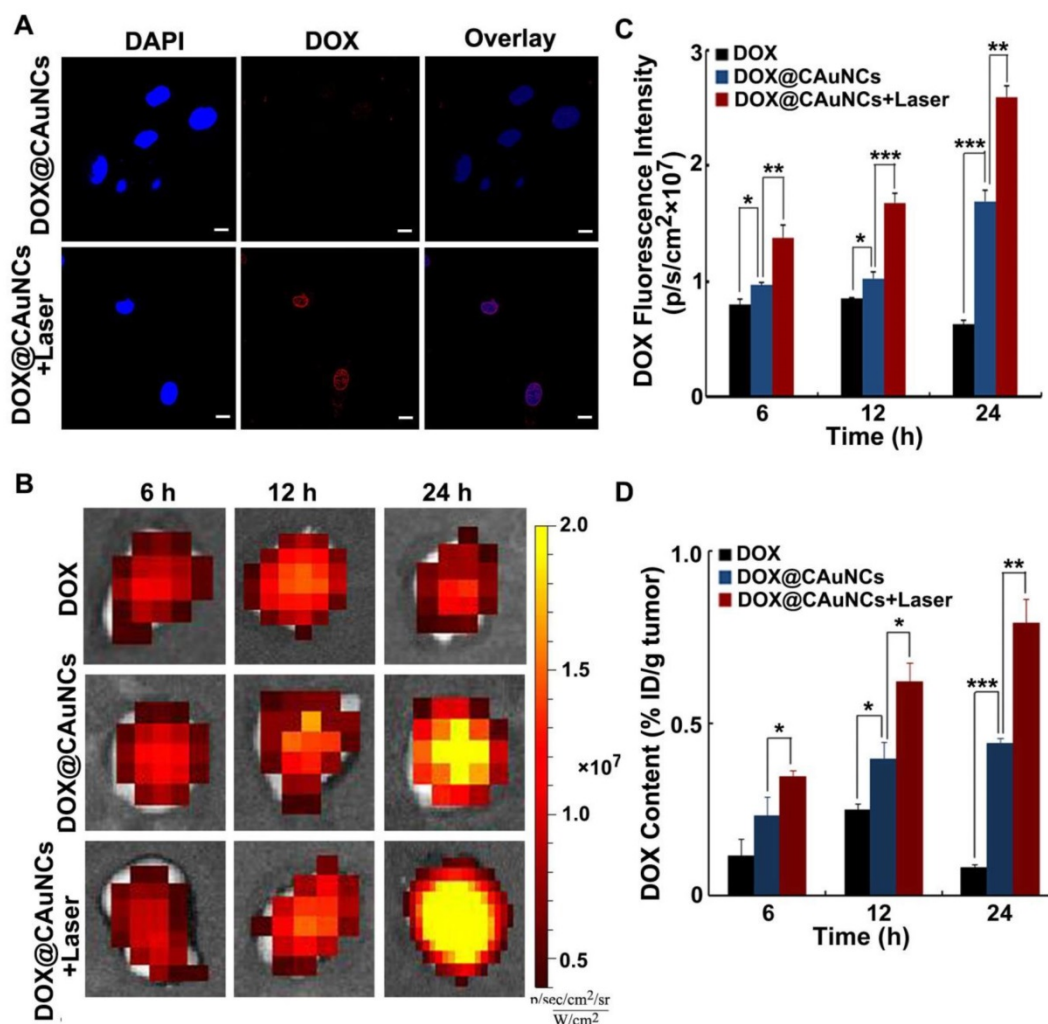


Figure 4. *In vivo* NIR laser-induced DOX release from DOX@CAuNCs. (A) Confocal microscopic images of H22 cells treated with DOX@CAuNCs for 8 h, followed by irradiation with or without 808 nm laser (1 W/cm^2) for 5 min. Scale bar: $10 \mu\text{m}$. (B) *Ex vivo* fluorescence imaging of DOX in tumor tissues of H22 tumor-bearing mice at different time intervals after intravenous injection with DOX or DOX@CAuNCs at DOX dose of 15 mg/kg , followed with or without 808 nm laser sequential irradiation (1 W/cm^2) for 10 min. (C) DOX fluorescence intensity in tumor tissues as indicated in B. (D) *In vivo* released DOX contents in tumor tissues as indicated in B by fluorescence spectrometer. Data as mean value \pm SD ($n=4$). * $P<0.05$, ** $P<0.01$, *** $P<0.001$.

In Vivo NIR Laser-Induced Drug Release of DOX@CAuNCs

To reveal NIR laser-controlled photothermal drug release, H22 cells were treated with DOX@CAuNCs for 8 h, followed with or without 808 nm laser irradiation for 5 min. Intracellular DOX fluorescence observation by confocal microscopy showed that faint DOX fluorescence was detected in DOX@CAuNCs-treated cells in the absence of NIR laser irradiation, while strong intracellular DOX fluorescence was displayed in DOX@CAuNCs-treated cells upon NIR laser irradiation and DOX was translocated to nucleus (Figure 4A). These results confirmed that NIR laser-induced hyperthermia accelerated DOX release from CAuNCs, which might exert synergistic PTT-chemotherapy.

The NIR laser-induced DOX release from DOX@CAuNCs was further confirmed in H22 tumor-bearing mice. The mice were intravenously injected with free DOX or DOX@CAuNCs. At 6, 12

and 24 h, the tumors of mice were sequentially irradiated with 808 nm laser and DOX fluorescence in the tumors was investigated by whole-animal fluorescence imaging (Figure 4B-C). DOX fluorescence in tumors of DOX@CAuNCs-treated mice significantly enhanced upon NIR laser irradiation at 6 h, suggesting *in vivo* NIR laser-induced DOX release. Meanwhile, DOX fluorescence in the tumors further increased after the second and third NIR laser irradiation at 12 and 24 h, respectively, demonstrating that multiple NIR laser irradiations further increased DOX release in tumors. The NIR laser-induced DOX release from DOX@CAuNCs was verified by determining the released DOX content in tumor tissues (Figure 4D), in which the released DOX content in tumors of DOX@CAuNCs-treated mice was 1.5-, 1.6- and 1.8-fold than that of non-irradiated groups after the first, second and third NIR laser irradiation at 6, 12 and 24 h, respectively.

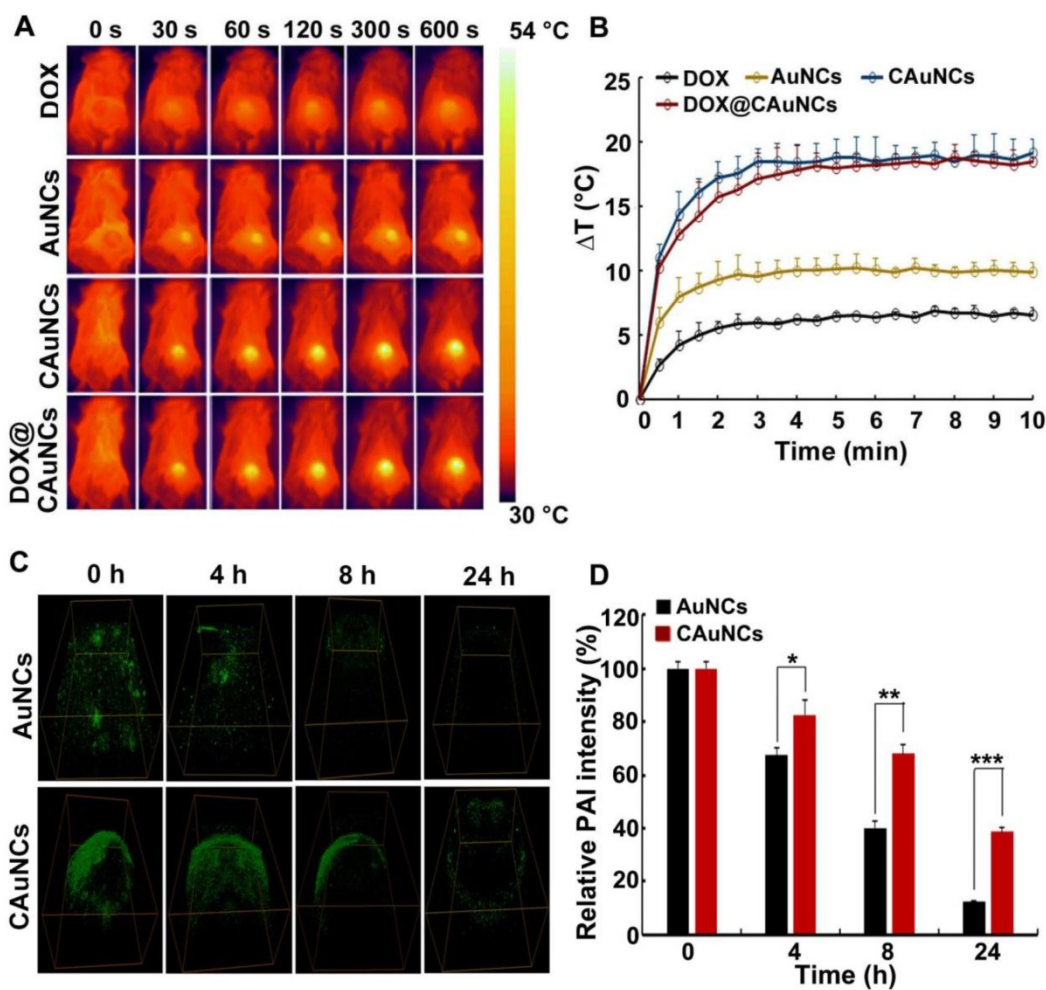


Figure 5. *In vivo* NIR laser-controlled photothermal effects and PAI capacity of DOX@CAuNCs. (A) Infrared thermography of tumor tissues of H22 tumor-bearing mice recorded by an IR camera at 24 h after intravenous injection with different formulations at Au dose of 10 mg/kg (the corresponding DOX dose was 15 mg/kg), followed with 808 nm laser irradiation (1 W/cm²) for different time intervals at the tumor sites. (B) Temperature change profiles of the above four NIR laser-irradiated groups. (C) *In vivo* PA imaging in H22 tumor-bearing mice at different time intervals after intratumoral injection with AuNCs or CAuNCs at Au dose of 10 mg/kg. (D) Relative photoacoustic intensity as indicated in C. Data as mean value \pm SD (n=3). *P<0.05, **P<0.01, ***P<0.001.

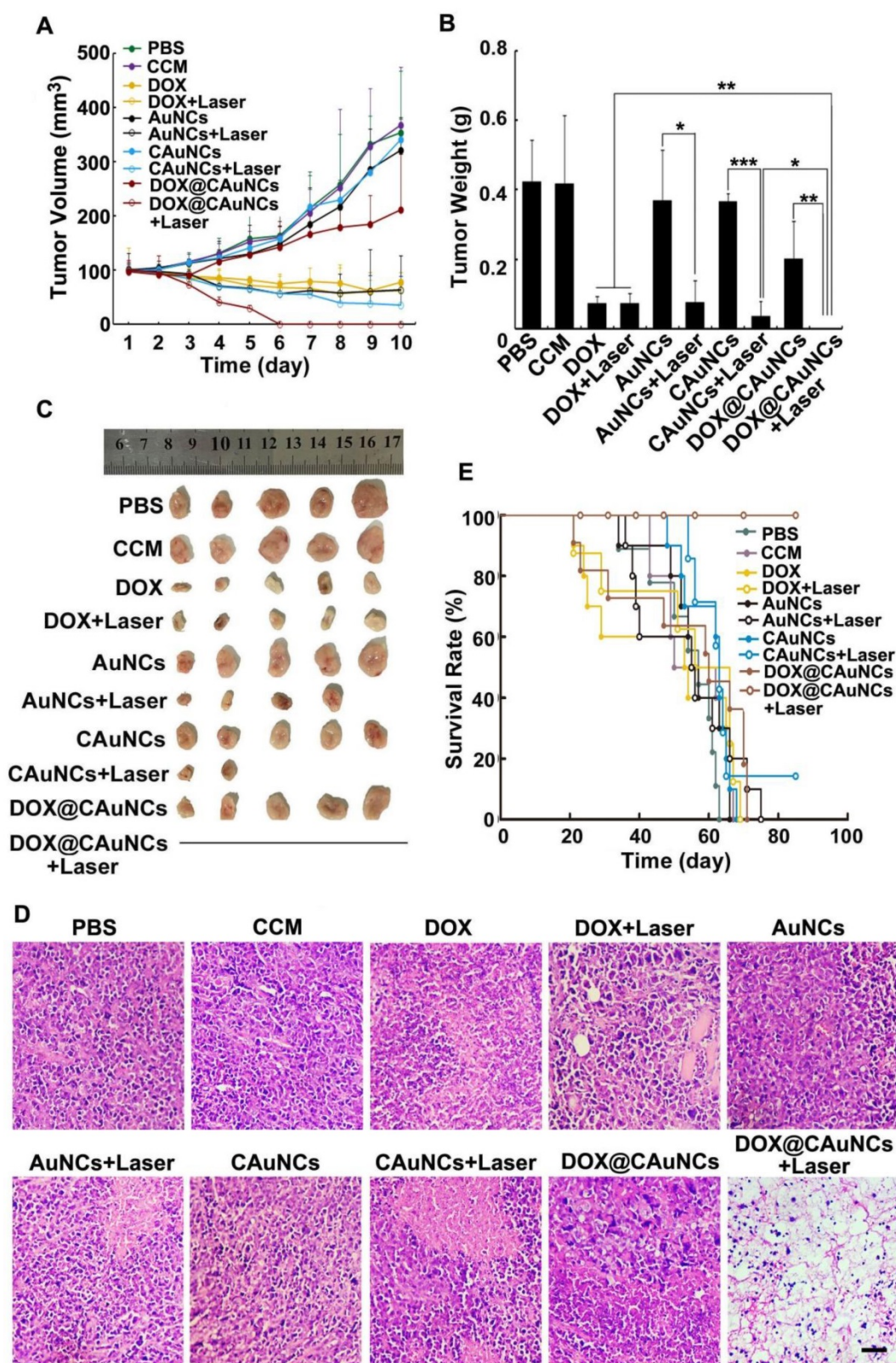


Figure 6. *In vivo* synergistic PTT-chemotherapy of DOX@CAuNCs. **(A)** Tumor growth curves of H22 tumor-bearing mice after intravenous injection with different formulations at the corresponding Au and DOX dose of 10 and 15 mg/kg, followed with or without 808 nm laser irradiation (1 W/cm²) for 10 min once a day for four consecutive days at the tumor tissues. Data as mean value±SD (n=13). **(B)** Tumor weight after treatment. Data as mean value ± SD (n=5). *P<0.05, **P<0.01, ***P<0.001. **(C)** Photos of tumors after treatment. **(D)** H&E staining of tumors after H22 tumor-bearing mice were intravenously injected with different formulations at the corresponding Au and DOX dose of 10 and 15 mg/kg, followed with or without 808 nm laser irradiation (1 W/cm²) for 10 min once a day for three consecutive days at the tumor tissues. Scale bar: 50 μm. **(E)** Kaplan-Meier survival plot of H22 tumor-bearing mice after intravenous injection with different formulations at the corresponding Au and DOX dose of 10 and 15 mg/kg, followed with or without 808 nm laser irradiation (1 W/cm²) for 10 min once a day for four consecutive days at the tumor tissues (n=8).

In Vivo Photothermal Effects and Synergistic PTT-Chemotherapy of DOX@CAuNCs

Considering the enhanced tumor accumulation of CAuNCs and DOX@CAuNCs, their *in vivo* photothermal effects were evaluated in H22 tumor-bearing mice. The mice were intravenously injected with DOX, AuNCs, CAuNCs or DOX@CAuNCs. At 24 h after injection, the tumor tissues were irradiated with 808 nm laser for different time intervals and their temperature was evaluated by an Infrared (IR) camera (Figure 5A-B). Compared with the irradiated AuNCs group, the irradiated CAuNCs and DOX@CAuNCs groups displayed a significant temperature rise curve in tumor tissues, which might be owing to their selective tumor targeting capacity. The maximal temperature of the irradiated CAuNCs and DOX@CAuNCs groups in tumor tissues can reach up to 52.5 °C, high enough to kill cancer cells. However, the maximal temperature of the irradiated DOX group, a negative control, only exhibited a slight increase.

The *in vivo* photoacoustic imaging (PAI) capacity of CAuNCs was further investigated. H22 tumor-bearing mice were intratumorally injected with AuNCs or CAuNCs, and PAI was performed at different time points on the same tumor sites of mice (Figure 5C-D). The photoacoustic signals of tumors of mice injected with CAuNCs were significantly higher than those with AuNCs, which suggested that coating with CCM increased the PAI capacity and retention of AuNCs in tumor tissues. To further confirm the enhanced retention of DOX@CAuNCs, H22 tumor-bearing mice were intravenously injected with free DOX, AuNCs, CAuNCs or DOX@CAuNCs. At 24 h after injection, the mice were or were not irradiated with 808 nm laser for 10 min and then repeated irradiation once a day. Consistently, 808 nm laser irradiation increased DOX release in tumor tissues of mice treated with DOX@CAuNCs (Figure S8B). Meanwhile, more AuNCs and DOX were detected in tumor tissues of mice treated with DOX@CAuNCs both in the presence or absence of 808 nm laser irradiation even after 72 and 96 h (Figure S8A-B). These results demonstrated that DOX@CAuNCs exhibited significantly improved tumor retention compared with AuNCs and free DOX.

To demonstrate *in vivo* precisely synergistic photothermal-chemotherapeutic anticancer activity of DOX@CAuNCs, H22 tumor-bearing mice were intravenously injected with PBS, CCM, DOX, AuNCs, CAuNCs or DOX@CAuNCs. At 24 h after injection, the tumor tissues of mice were subjected to or not to irradiation with 808 nm laser for 10 min and then repeated irradiation once every day for four

consecutive days (Figure 6A-C). The tumors of mice treated with PBS, CCM, AuNCs or CAuNCs grew fast and exhibited the similar tumor growth curves. Almost same tumor inhibition was detected in free DOX-treated group in the presence or absence of 808 nm laser irradiation, confirming that NIR laser irradiation itself had a negligible influence on tumor growth. Even though AuNCs and CAuNCs achieved significantly enhanced anticancer efficacy upon 808 nm laser irradiation, not all of the tumors were eliminated. However, DOX@CAuNCs displayed a complete tumor eradication upon 808 nm laser irradiation without any recurrence after 10 days treatment, illustrating an excellent anticancer activity due to synergistic PTT-chemotherapy. Moreover, histological analysis by hematoxylin and eosin (H&E) staining demonstrated severe tumor necrosis with worst structural destruction in tumors of mice injected with DOX@CAuNCs upon NIR laser irradiation (Figure 6D), further confirming that DOX@CAuNCs exhibited the strongest synergistic photothermal-chemotherapeutic anticancer activity. The survival rate of the mice also showed the same trend (Figure 6E). Prolonged survival time was observed in mice injected with DOX@CAuNCs upon NIR laser irradiation, almost 100% of mice alive after 85 days when all mice in other groups had died. Although administration of free DOX caused a body weight loss that returned to normal after 10 days, DOX@CAuNCs in the presence or absence of NIR laser irradiation did not significantly affect the body weight of H22 tumor-bearing mice compared with PBS (Figure S9). Meanwhile, the histopathological examinations of major organs by H&E staining showed that heart and kidney were damaged in DOX-treated group both with or without NIR laser irradiation, while no obvious pathological changes in heart, liver, spleen, lung and kidney were detected in DOX@CAuNCs-treated group even with NIR laser irradiation (Figure 7), revealing the good biosafety of DOX@CAuNCs.

Pro-Inflammatory Response of AuNCs Coating with CCM

Nanoparticles were reported to induce inflammatory response after phagocytosis by RES [35]. Considering that CCM coating significantly decreased the phagocytosis of AuNCs by macrophages, their pro-inflammatory response in macrophages was first evaluated. Raw264.7 cells were treated with AuNCs or CAuNCs for 12 h, and then the pro-inflammatory gene expression was determined by quantitative real time reverse transcription-polymerase chain reaction (RT-PCR) (Figure 8A). As expected, AuNCs markedly increased the expression

of pro-inflammatory genes, such as Interleukin (IL)-1 β , IL-6 and inducible nitric oxide synthase (iNOS). However, the expression of these pro-inflammatory genes induced by CAuNCs was significantly lower than that induced by AuNCs, suggesting that CCM coating decreased AuNCs-induced pro-inflammatory response. Furthermore, *in vivo* inflammatory response was evaluated in serum of BALB/c mice at 24 h after intravenous injection with PBS, AuNCs or CAuNCs by enzyme-linked immunosorbent assay (ELISA) analysis (Figure 8B). Consistently, AuNCs significantly increased IL-1 β and IL-6 contents in serum, while the contents of these pro-inflammatory genes significantly decreased in CAuNCs-treated group compared with AuNCs-treated group. These results revealed that coating with CCM could decrease the inflammatory response induced by AuNCs, which further revealed the good biosafety of DOX@CAuNCs.

Conclusions

In summary, we have fabricated a biomimetic AuNCs-based platform coated with CCM for highly loading anticancer drug DOX by transmembrane ammonium sulfate gradient method. DOX@CAuNCs exhibit strong photothermal conversion capacity and on-demand DOX release upon NIR laser irradiation. Furthermore, DOX@CAuNCs display decreased macrophage phagocytosis, prolonged blood circulation and enhanced cellular uptake by cancer cells, leading to remarkable tumor targeting capacity. These superior performances of DOX@CAuNCs generate spatial-temporal synchronization of PTT-chemotherapy and the highly efficient tumor ablation with no obvious side effects. In addition, CCM coating decreases AuNCs-induced inflammatory reaction *in vivo*. This finding might provide a new opportunity for achieving desired therapeutic effects in cancer treatment by using precisely synergistic PTT-chemotherapy.

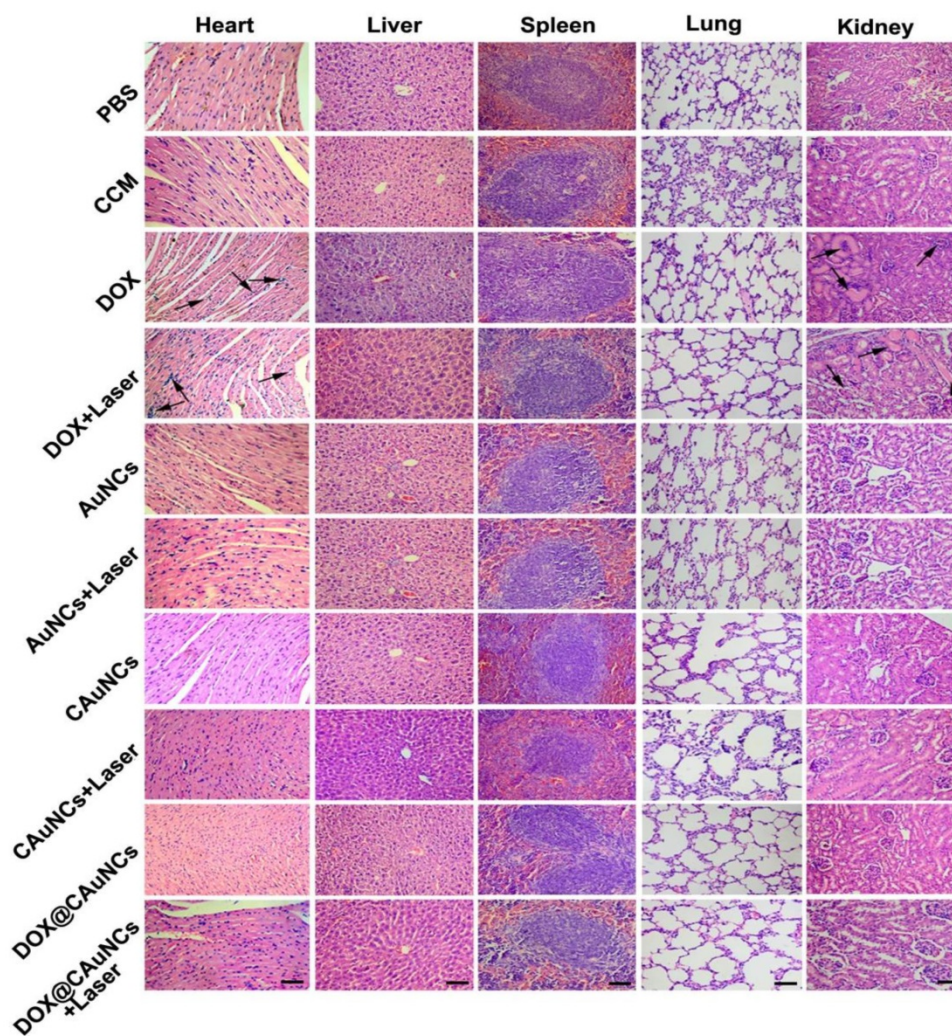


Figure 7. Histological observation of tissues of H22 tumor-bearing mice after intravenous injection with different formulations at the corresponding Au and DOX dose of 10 and 15 mg/kg, followed with or without 808 nm laser irradiation (1 W/cm²) for 10 min once a day for four consecutive days at the tumor tissues by H&E staining. Scale bar: 50 μ m.

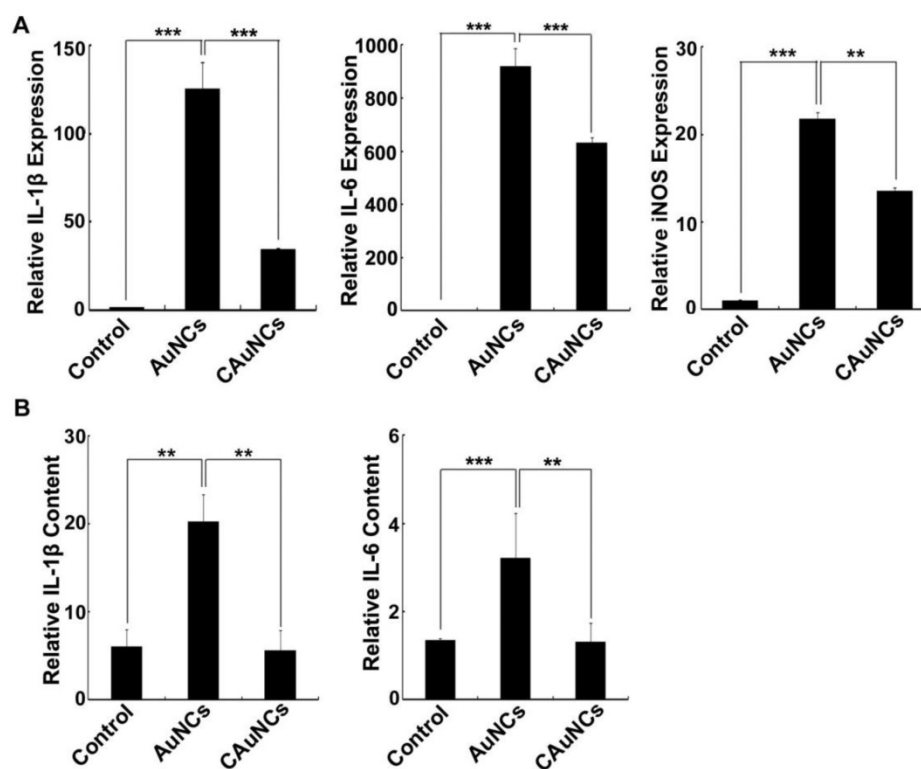


Figure 8. Effects of CCM coating on AuNCs-induced Inflammation. **(A)** The expression of IL-1 β , IL-6 and iNOS in RAW264.7 cells treated with PBS, AuNCs or CAuNCs at Au concentration of 10 μ g/mL for 24 h by quantitative RT-PCR analysis. **(B)** IL-6 and IL-1 β contents in serum of BALB/c mice at 24 h after intravenous injection with PBS, AuNCs or CAuNCs at Au dose of 10 mg/kg. Data as mean value \pm SD (n=4). **P<0.01. ***P<0.001.

Materials and Methods

Materials

Ethylene glycol and 4'-diamidino-2-phenylindole (DAPI) were purchased from Sinopharm Chemical Reagent Co. Ltd (Beijing, China). NaSH, CF₃COOAg, HAuCl₄ and poly(vinylpyrrolidone) (PVP, average Mr=55,000) were purchased from Sigam-Aldrich Corp (St Louis, MO, USA). Doxorubicin hydrochloride (DOX HCl, with the purity of above 98.0%) was obtained from Beijing Huafeng United Technology CO., Ltd. (Beijing, China). RPMI 1640, DMEM and fetal bovine serum (FBS) were purchased from Gibco BRL/Life Technologies (Grand Island, NY, USA). CCK-8 reagent was obtained from Dojindo Molecular Technologies, Inc. (Tokyo, Japan). Rabbit anti-mouse β -actin monoclonal antibody, rabbit anti-mouse CD47 polyclonal antibody and rabbit anti-mouse CD54 monoclonal antibody were purchased from Cell Signaling Technology (Danvers, MA, USA). TRIzol reagent was purchased from Thermo Fisher Scientific, Inc. (Waltham, MA, USA). PrimeScript RT reagent kit and SYBR Green Supermix were obtained from Takara Bio Inc. (Kusatsu, Japan). All other reagents were of analytical grade and used without any further purification.

Cell Lines and Animals

Murine hepatocarcinoma cell line H22 and murine macrophage cell line RAW264.7 were purchased from Type Culture Collection of Chinese Academy of Sciences (Shanghai, China). H22 cells were cultured in RPMI 1640 medium and RAW264.7 cells were cultured in DMEM medium containing 10% FBS, 100 U/mL penicillin and 100 μ g/mL streptomycin at 37 °C in a 5% CO₂ humidified incubator. Sprague Dawley (SD) male rats (6-8 weeks) and BALB/c male mice (6 weeks, 20-22 g) were provided by Hubei Provincial Center for Disease Control and Prevention (Wuhan, China). H22 tumor-bearing mice were constructed by subcutaneous injection of 2 \times 10⁶ H22 cells into the flanks of BALB/c mice. All animal experiments were approved by the Institutional Animal Care and Use Committee at Tongji Medical College, Huazhong University of Science and Technology (Wuhan, China).

AuNCs Synthesis

AuNCs were synthesized by using a galvanic replacement reaction between Ag nanocubes and HAuCl₄ as the template as described [27]. Briefly, Ag nanocubes were first synthesized as followed. Ethylene glycol (10 mL) was heated in oil bath up to

150 °C for 40 min under magnetic stirring. 120 µL of NaSH solution (3 mM in ethylene glycol) was quickly added into hot ethylene glycol, followed by adding 2.5 mL of PVP (25 mg PVP in 13 mL ethylene glycol) and 0.8 mL of CF₃COOAg solution (282 mM in ethylene glycol). The reaction was maintained at 150 °C for 25 min. The obtained Ag nanocubes were washed with acetone and deionized water, and then stored in deionized water. Furthermore, Ag nanocubes (200 mM) were added to 600 mL of deionized water containing 0.8 mg/mL PVP and heated up to 100 °C in oil bath for 45 min under magnetic stirring. Then, HAuCl₄ aqueous solution (1 mM) was injected at the rate of 0.2 mL/min until the solution had an LSPR peak at 800 nm monitored by UV-Vis-NIR spectroscopy (TU 1901, Beijing Tongyong General Instrumental Co, Ltd., Beijing, China). The AuNCs were collected by centrifugation at 15,000g for 15 min, washed with deionized water three times and then dispersed in phosphate buffer saline (PBS) for later experiments. The content of Au element was measured by ICP-OES (model Optima 4300 DV, PerkinElmer, Norwalk, CT, USA).

Preparation of CAuNCs

To construct CAuNCs, CCM derived from H22 cells were first collected as described [25,26]. Briefly, the harvested H22 cells were suspended in hypotonic lysis buffer (pH 7.4, containing 18 mM Tris-HCl, 9 mM KCl, 1.5 mM MgCl₂ and one EDTA-free mini protease inhibitor tablet), followed by freezing at -80 °C, thawing at room temperature and disrupting by using bath ultrasonic cleaner at a fixed frequency of 42 kHz and power of 100 W. The supernatants were centrifuged at 3,000g for 6 min to remove debris, then centrifuged at 20,000g for 25 min to remove intracellular contents and 120,000g for 1 h to collect cell membrane pellets. Furthermore, the mixture of AuNCs (5 µg/mL) and H22 CCM (15 µg/mL protein) was suspended in PBS and then extruded through a 200 nm polycarbonate porous membrane for 11 times, followed by centrifugation at 15,000g for 15 min to collect CAuNCs. The resulting CAuNCs were washed with PBS.

Preparation and Characterization of DOX@CAuNCs

AuNCs (5 µg/mL) were dispersed in 240 mM ammonium sulfate solution (pH 7.4) and magnetically stirred for 24 h. H22 CCM (15 µg/mL protein) was added and then the mixture was extruded through a 200 nm polycarbonate porous membrane for 11 times to acquire CAuNCs loaded with ammonium sulfate. The excess CCM and exterior ammonium sulfate solution were removed by centrifugation at 15,000g

for 15 min. Different amounts of DOX was added to CAuNCs and stirred at 37 °C for 12 h. The unloaded DOX was removed by centrifugation at 15,000g for 15 min and then washed with PBS three times to obtain DOX@CAuNCs.

The hydrodynamic diameter and zeta potential of AuNCs, CAuNCs and DOX@CAuNCs were measured using DLS (ZetaSizer ZS90, Malvern Instrument, UK). The morphology of AuNCs, CAuNCs and DOX@CAuNCs was observed by TEM (Tecnai G2-20, FEI, Netherlands). The UV-Vis-NIR absorption spectra of CCM, AuNCs, CAuNCs and DOX@CAuNCs in PBS were measured using a UV-Vis-NIR spectrometer. Drug loading capacity (DLC) and encapsulation efficiency (EE) of DOX@CAuNCs were defined by the following equations:

$$\text{DLC}(\%) = \left(\frac{W_{\text{encapsulated DOX in DOX@CAuNCs}}}{W_{\text{DOX@CAuNCs}}} \right) \times 100;$$

$$\text{EE}(\%) = \left(\frac{W_{\text{encapsulated DOX in DOX@CAuNCs}}}{W_{\text{total input DOX}}} \right) \times 100.$$

The encapsulated DOX was determined by dispersing DOX@CAuNCs in PBS and then irradiating at 808 nm laser (1 W/cm²) for 5 min for 12 times until there was no further fluorescence signal in the supernatants. DOX fluorescence in the supernatants was measured by a Hitachi F-4500 fluorescence spectrometer (Tokyo, Japan).

Passive Loading DOX into CAuNCs (DOX_{passive}@CAuNCs)

As a control, DOX_{passive}@CAuNCs was prepared by a passive loading method. Briefly, DOX solution (20 µg/mL) was added into AuNCs (5 µg/mL) and then mixed by magnetic stirring at 37 °C for 24 h. The supernatants were centrifuged at 15,000g for 15 min and washed with PBS to obtain DOX@AuNCs. Then, H22 CCM (15 µg/mL protein) was added into DOX@AuNCs solution and extruded through 200 nm polycarbonate porous membrane for 11 times. The excess CCM was removed by centrifugation at 15,000g for 15 min and washed with PBS three times to obtain DOX_{passive}@CAuNCs.

Western Blotting

H22 whole cells, H22 CCM, CAuNCs and DOX@CAuNCs were lysed in RIPA lysis buffer. The proteins were separated on 10% sodium dodecyl sulfate-polyacrylamide gel (SDS-PAGE) and transferred to polyvinylidene difluoride (PVDF) membranes. The membranes were blocked with 5% bovine serum albumin (BSA), incubated with primary antibodies including anti-CD47, anti-CD54 and anti-β-actin at 4 °C overnight, washed with Tris-

buffered saline with 0.1% Tween-20 (TBST) and incubated with horseradish peroxidase-conjugated secondary immunoglobulin G at room temperature for 1 h. The protein bands were detected using enhanced chemiluminescence on ChemiDoc XRS Gel image system (Bio-Rad, Hercules, CA, USA) [36].

In Vitro Photothermal Effects

AuNCs, CAuNCs and DOX@CAuNCs at Au concentration of 10 $\mu\text{g}/\text{mL}$ were dispersed in 0.5 mL of PBS. The dispersions were then irradiated with 808 nm laser (1 W/cm²) for different time intervals. The temperature was monitored by FLIR E50 IR camera (FLIR Systems Inc., USA). PBS, H22 CCM and DOX were used as negative controls.

In Vitro Photothermal Stability

AuNCs, CAuNCs and DOX@CAuNCs at Au concentration of 10 $\mu\text{g}/\text{mL}$ were dispersed in 0.5 mL of PBS. The dispersions were then irradiated with 808 nm laser (1 W/cm²) for 13 min and then cooled at ambient temperature for 7 min. The irradiation-cooling cycles were repeated for four times and the temperature was recorded by FLIR E50 IR camera.

In Vitro NIR Laser-Induced DOX Release from DOX@CAuNCs

DOX@CAuNCs at Au concentration of 1 mg/mL were dispersed in a 1.5 mL centrifuge tube. The dispersions were then irradiated with or without 808 nm laser (1 W/cm²) for 5 min at the designated time points, followed by centrifugation at 15,000g for 15 min. The supernatants were collected and the pellets were resuspended in 1 mL of PBS for the next irradiation with or without 808 nm laser (1 W/cm²) for 5 min. DOX fluorescence in supernatants was measured by fluorescence spectrometer.

Macrophage Escape

Macrophage RAW264.7 cells were seeded in a 12-well plate at a density of 2×10^5 cells/well overnight. The cells were then treated with AuNCs, CAuNCs or DOX@CAuNCs at Au concentration of 10 $\mu\text{g}/\text{mL}$ in the presence or absence of FBS for different time intervals. Subsequently, the cells were washed with PBS three times and then dissolved in *Aqua Regia* (containing HNO₃:HCl=1:3, v/v). The intracellular Au contents were determined by ICP-OES.

In Vivo Pharmacokinetics

SD male rats were randomly divided into three groups (n=4 per group). The rats were intravenously injected with AuNCs, CAuNCs or DOX@CAuNCs at Au dose of 10 mg/kg. At the designed time points, 200 μL of blood was collected from orbits, dissolved in *Aqua Regia* and Au contents were then determined by

ICP-OES.

Cellular Uptake by Cancer Cells

H22 cells were seeded in 12-well plates at a density of 1×10^5 cells/well overnight. The cells were then treated with AuNCs, CAuNCs or DOX@CAuNCs at Au concentration of 10 $\mu\text{g}/\text{mL}$ in the presence or absence of FBS for different time intervals. The cells were washed with PBS three times and then dissolved in *Aqua Regia*. The intracellular Au contents were determined by ICP-OES.

Endocytic Pathway

H22 cells were pretreated with 50 μM EIPA (1 h), 10 $\mu\text{g}/\text{mL}$ CPZ (30 min) or 10 mM M β CD (30 min), respectively. The cells were then treated with DOX@CAuNCs at Au concentration of 10 $\mu\text{g}/\text{mL}$ in the presence of the above inhibitors for another 4 h. The cells were washed with PBS three times and then dissolved in *Aqua Regia*. The intracellular Au contents were determined by ICP-OES.

In Vitro Cytotoxicity against Cancer Cells

H22 cells were seeded in a 96-well plate at a density of 9×10^3 cells/well overnight. The cells were then treated with CCM, DOX, AuNCs, CAuNCs or DOX@CAuNCs at Au concentration of 10 $\mu\text{g}/\text{mL}$ (the corresponding DOX concentration was 1.5 $\mu\text{g}/\text{mL}$) for 12 h. The cells were washed with PBS and then irradiated with or without 808 nm laser (1 W/cm²) for 5 min at 37 °C. The cells were further incubated for 8 h and cell viability was determined using CCK-8 kit according to the manufacturer's guidance.

In Vivo Biodistribution

When tumor volume of H22 tumor-bearing mice grew up to 100-150 mm³, the mice were randomly divided into three groups (n=4 per group) and then intravenously injected with 0.1 mL of AuNCs, CAuNCs or DOX@CAuNCs at Au dose of 10 mg/kg. At 48 h post-injection, the mice were sacrificed, and their major organs (heart, liver, spleen, lung and spleen) and tumors were collected and completely digested with *Aqua Regia*. Au contents were determined by ICP-OES and expressed as percent of the injected AuNCs dose per gram of tissue.

NIR Laser-Induced Intracellular Drug Release

H22 cells were seeded in a 24-well plate at a density of 1×10^4 cells/well overnight and then treated with DOX@CAuNCs at Au concentration of 10 $\mu\text{g}/\text{mL}$. After 8 h incubation, the cells were washed with PBS and then irradiated with or without 808 nm laser (1 W/cm²) for 5 min. The cells were stained with 2.5 $\mu\text{g}/\text{mL}$ DAPI for 15 min at 37 °C and then observed under an Andor Revolution spinning disk

confocal microscope (Andor Technology, Belfast, UK).

NIR Laser-Induced Drug Release *in Vivo*

When tumor volume of H22 tumor-bearing mice grew up to 100-150 mm³, the mice were randomly divided into three groups (n=12) and then intravenously injected with DOX or DOX@CAuNCs at DOX dose of 15 mg/kg (the corresponding Au dose was 10 mg/kg). At 6 h after injection, the tumors injected with DOX@CAuNCs were irradiated with or without 808 nm laser (1 W/cm²) for 10 min. 1/3 of mice were sacrificed, and the left mice were or were not subjected to the second or third irradiation at 12 or 24 h at the tumor sites, respectively and then sacrificed. The tumors were collected and imaged by a Caliper IVIS Lumina II *in vivo* imaging system (PerkinElmer, Waltham, MA, USA). Furthermore, the tumors were homogenized in methanol, followed by centrifugation at 20,000g for 15 min to collect the supernatants. DOX contents were measured by fluorescence spectrometer and expressed as percent of the injected DOX dose per gram of tumor.

***In Vivo* PAI Imaging**

When tumor volume of H22 tumor-bearing mice grew up to 100-150 mm³, the mice were intratumorally injected with AuNCs or CAuNCs at Au dose of 10 mg/kg. At different time intervals, the mice were scanned on a homemade photoacoustic system to collect the photoacoustic signals [37,38]. The wavelength of laser was 744 nm and the laser energy per pulse was 200 nJ.

***In Vivo* Retention of DOX@CAuNCs**

When tumor volume of H22 tumor-bearing mice reached 100-150 mm³, the mice were intravenously injected with free DOX, AuNCs, CAuNCs or DOX@CAuNCs at Au dose of 10 mg/kg (the corresponding DOX dose was 15 mg/kg). At 24 h after injection, the mice were or were not irradiated with 808 nm laser (1 W/cm²) for 10 min and then repeated irradiation once a day. At 72 and 96 h, the mice were sacrificed and the tumors were harvested. Au contents were determined by digesting the tumors using *Aqua Regia* and then measuring by ICP-OES. DOX contents were determined by homogenizing the tumors in methanol, followed by centrifugation at 20,000g for 15 min to collect the supernatants and then measurement by fluorescence spectrometer.

***In Vivo* Photothermal Effect**

When tumor volume of H22 tumor-bearing mice grew up to 100-150 mm³, the mice were randomly divided into four groups (n=3 per group) and then intravenously injected with free DOX, AuNCs, CAuNCs or DOX@CAuNCs at Au dose of 10 mg/kg

(the corresponding DOX dose was 15 mg/kg). At 24 h after injection, the mice were irradiated with 808 nm laser (1 W/cm²) for different time intervals. Infrared thermography and the temperature of tumor tissues were simultaneously monitored by FLIR E50 IR camera.

***In Vivo* Anticancer Effect**

When tumor volume of H22 tumor-bearing mice grew up to 100-150 mm³, the mice were randomly divided into ten groups (n=13 per group) and then intravenously injected with PBS, CCM, DOX, AuNCs, CAuNCs or DOX@CAuNCs at Au dose of 10 mg/kg (the corresponding DOX dose was 15 mg/kg). At 24 h after injection, the mice were or were not irradiated with 808 nm laser (1 W/cm²) for 10 min and then repeated irradiation once a day for four consecutive days. The body weights were measured by using a scale-balance, and tumor lengths and widths were measured with a caliper every day. Tumor volume was calculated by the following equation: $V = (\text{tumor length}) \times (\text{tumor width})^2 / 2$. On day 11 after treatment, 5 mice each group were sacrificed. Tumors were collected and weighed, and other major organs (heart, liver, spleen, lung and kidney) were harvested and fixed in a 4% paraformaldehyde for H&E staining analysis. The rest mice were used for long-term survival observation.

***In Vivo* Histological Analysis of Tumors**

When tumor volume of H22 tumor-bearing mice grew up to 100-150 mm³, the mice were randomly divided into ten groups and then intravenously injected with PBS, CCM, DOX, AuNCs, CAuNCs or DOX@CAuNCs at Au dose of 10 mg/kg (the corresponding DOX dose was 15 mg/kg). At 24 h after injection, the mice were or were not irradiated with 808 nm laser (1 W/cm²) for 10 min and then repeated irradiation once a day for three consecutive days. On day 5 after treatment, the mice were sacrificed, and tumors were harvested and fixed in a 4% paraformaldehyde for H&E staining analysis.

Inflammatory Cytokine Expression in RAW264.7 Cells

RAW264.7 macrophage cells were seeded in a 6-well plate at a density of 2×10^5 cells/well overnight. The cells were treated with PBS, AuNCs or CAuNCs at Au concentration of 10 $\mu\text{g/mL}$. After 24 h treatment, the cells were washed with PBS and harvested for the expression analysis of IL-1 β , IL-6 and iNOS by quantitative RT-PCR. Briefly, total cellular RNAs were isolated from the cells using TRIzol reagent according to the manufacturer's guidance. The mRNAs were then transcribed to cDNAs using PrimeScript RT reagent kit. The qPCR

reactions were carried out using a SYBR Green Supermix on an ABI Step One Plus system (Applied Biosystems, Foster City, CA, USA). The sequence of primers was as follows: sense 5'-TGCCACCTTT TGACAGTGATG-3' and anti-sense 5'-TGATGTGC TGCTGCGAGA TT-3' for IL-1 β ; sense 5'-CCTGAGA CTCAAGCAGAAATTGG-3' and anti-sense 5'-AGAA GGAAGGTCGGCTTCAGT-3' for IL-6; sense 5'-GATGTTGAACTATGTCCTATC TCC-3' and anti-sense 5'-GAACACCACCTTTCACCAAGAC-3' for iNOS; sense 5'-GTTCTACCCCAATGTGTCC-3' and anti-sense 5'-TAGCCCAAGATGCCCTTC AGT-3 for glyceraldehyde-3-phosphate dehydrogenase (GAPDH). The PCR reaction was performed under the following conditions: initial denaturation at 95 °C for 1 min, followed by 40 cycles of 95 °C for 15 sec, 60 °C for 1 min, and with a final extension step at 95 °C for 15 sec. The relative gene expression levels of IL-1 β , IL-6 and iNOS were analyzed using the 2^{- $\Delta\Delta$ Ct} method [39].

In Vivo Inflammatory Cytokine Activity

BALB/c mice was randomly divided into three groups and intravenously injected with PBS, AuNCs or CAuNCs at Au dose of 10 mg/kg. After 24 h treatment, the blood was collected and the plasma was separated for analysis of IL-1 β and IL-6 activity by ELISA.

Statistical Analysis

All experiments were carried out at least three times. Statistical analysis was carried out using Student's *t*-test. *P* < 0.05 was considered statistically significant.

Supplementary Material

Supplementary figures and tables.
<http://www.thno.org/v08p5362s1.pdf>

Acknowledgements

This work was supported by National Basic Research Program of China (2018YFA0208903 and 2015CB931802), National Natural Science Foundation of China (81672937, 81473171, 81773653 and 81627901) and Program for Changjiang Scholars and Innovative Research Team in University (IRT13016). We thank the Analytical and Testing Center of Huazhong University of Science and Technology for related analysis.

Competing Interests

The authors have declared that no competing interest exists.

References

- Yang Y, Liu J, Liang C, et al. Nanoscale metal-organic particles with rapid clearance for magnetic resonance imaging-guided photothermal therapy. *ACS Nano*. 2016; 10: 2774-2781.
- Huang P, Lin J, Li W, et al. Biodegradable gold nanovesicles with an ultrastrong plasmonic coupling effect for photoacoustic imaging and photothermal therapy. *Angew Chem Int Ed Engl*. 2013; 125: 14208-14214.
- Ahmed M, Brace CL, Lee FJr, et al. Principles of and advances in percutaneous ablation. *Radiology*. 2011; 258: 351-369.
- Paulet E, Aubé C, Pessaux P, et al. Factors limiting complete tumor ablation by radiofrequency ablation. *Cardiovasc Intervent Radiol*. 2008; 31: 107-115.
- Chu KF, Dupuy DE. Thermal ablation of tumours: Biological mechanisms and advances in therapy. *Nat Rev Cancer*. 2014; 14: 199-208.
- Wang L, Lin X, Wang J, et al. Novel insights into combating cancer chemotherapy resistance using a plasmonic nanocarrier: enhancing drug sensitiveness and accumulation simultaneously with localized mild photothermal stimulus of femtosecond pulsed laser. *Adv Funct Mater*. 2014; 24: 4229-4239.
- Gormley AJ, Larson N, Sadekar S, et al. Guided delivery of polymer therapeutics using plasmonic photothermal therapy. *Nano Today*. 2012; 7: 158-167.
- Yang X, Liu X, Liu Z, et al. Near-infrared light-triggered, targeted . *ACS Appl Mater Interfaces*. 2017; 9: 23564-23573.
- Dong K, Liu Z, Li Z, et al. Hydrophobic anticancer drug delivery by a 980 nm laser-driven photothermal vehicle for efficient synergistic therapy of cancer cells in vivo. *Adv Mater*. 2013; 25: 4452-4458.
- Li F, Yang H, Bie N, et al. Zwitterionic temperature/redox-sensitive nanogels for near-infrared light-triggered synergistic thermo-chemotherapy. *ACS Appl Mater Interfaces*. 2017; 9: 23564-23573.
- Li Y, Deng Y, Tian X, et al. Multipronged design of light-triggered nanoparticles to overcome cisplatin resistance for efficient ablation of resistant tumor. *ACS Nano*. 2015; 9: 9626-9637.
- Li Y, Liu G, Ma J, et al. Chemotherapeutic drug-photothermal agent co-self-assembling nanoparticles for near-infrared fluorescence and photoacoustic dual-modal imaging-guided chemo-photothermal synergistic therapy. *J Control Release*. 2017; 258: 95-107.
- Zhang L, Chen Y, Li Z, et al. Tailored synthesis of octopus-type Janus nanoparticles for synergistic actively-targeted and chemo-photothermal therapy. *Angew Chem Int Ed Engl*. 2016; 55: 2118-2121.
- Piao JG, Wang L, Gao F, et al. Erythrocyte membrane is an alternative coating to polyethylene glycol for prolonging the circulation lifetime of gold nanocages for photothermal therapy. *ACS Nano*. 2014; 8: 10414-10425.
- Wang Z, Chen Z, Liu Z, et al. A multi-stimuli responsive gold nanocages-hyaluronic platform for targeted photothermal and chemotherapy. *Biomaterials*. 2014; 35: 9678-9688.
- Skrabalak SE, Chen J, Au L, et al. Gold nanocages for biomedical applications. *Adv Mater*. 2007; 19:3177-3184.
- Ibrahim KE, Bakhiet AO, Awadalla ME, et al. A priming dose protects against gold nanoparticles-induced proinflammatory cytokines mRNA expression in mice. *Nanomedicine (Lond)*. 2018; 13: 313-323.
- Chen J, Wang D, Xi J, et al. Immuno gold nanocages with tailored optical properties for targeted photothermal destruction of cancer cells. *Nano Lett*. 2007; 7: 1318-1322.
- Au L, Zheng D, Zhou F, et al. A quantitative study on the photothermal effect of immuno gold nanocages targeted to breast cancer cells. *ACS Nano*. 2008; 2: 1645-1652.
- Yavuz MS, Cheng Y, Chen J, et al. Gold nanocages covered by smart polymers for controlled release with near-infrared light. *Nat Mater*. 2009; 8: 935-939.
- Li W, Cai X, Kim C, et al. Gold nanocages covered with Thermally-Responsive Polymers for Controlled Release by High-Intensity Focused Ultrasound. *Nanoscale*. 2011; 3: 1724-1730.
- Moon GD, Choi SW, Cai X, et al. A new theranostic system based on gold nanocages and phase-change materials with unique features for photoacoustic imaging and controlled release. *J Am Chem Soc*. 2011; 133: 4762-4765.
- Shi P, Qu K, Wang J, et al. pH-responsive NIR enhanced drug release from gold nanocages possesses high potency against cancer cells. *Chem Commun*. 2012; 48: 7640-7642.
- Palivan CG, Goers R, Najer A, et al. Bioinspired polymer vesicles and membranes for biological and medical applications. *Chem Soc Rev*. 2016; 45: 377-411.
- Rao L, Bu LL, Cai B, et al. Cancer cell membrane-coated upconversion nanoprobe for highly specific tumor imaging. *Adv Mater*. 2016; 28: 3460-3466.
- Chen Z, Zhao P, Luo Z, et al. Cancer cell membrane-biomimetic nanoparticles for homologous-targeting dual-modal imaging and photothermal therapy. *ACS Nano*. 2016; 10: 10049-10057.
- Skrabalak SE, Au L, Li X, et al. Facile synthesis of Ag nanocubes and Au nanocages. *Nat Protoc*. 2007; 2: 2182-2190.
- Barenholz, Y. Liposome application: Problems and prospects. *Curr Opin Colloid Interface Sci*. 2001; 6: 66-77.
- Barenholz, Y. Doxil®-the first FDA-approved nano-drug: lessons learned. *J Control Release*. 2012; 160: 117-134.

30. Hu CM, Fang RH, Luk BT, et al. 'Marker-of-self' functionalization of nanoscale particles through a top-down cellular membrane coating approach. *Nanoscale* 2013; 5: 2664–2668.
31. Jaiswal S, Jamieson CH, Pang WW, et al. CD47 is upregulated on circulating hematopoietic stem cells and leukemia cells to avoid phagocytosis. *Cell*. 2009; 138: 271–285.
32. Rodriguez PL, Harada T, Christian DA, et al. Minimal "Self" peptides that inhibit phagocytic clearance and enhance delivery of nanoparticles. *Science*. 2013; 339: 971–975.
33. Lawson C, Wolf S. ICAM-1 signaling in endothelial cells. *Pharmacol Rep*. 2009; 61: 22–32.
34. Zhu JY, Zheng DW, Zhang MK, et al. Preferential cancer cell self-recognition and tumor self-targeting by coating nanoparticles with homotypic cancer cell membranes. *Nano Lett*. 2016; 16: 5895–5901.
35. Park EJ, Park K. Oxidative stress and pro-inflammatory responses induced by silica nanoparticles in vivo and in vitro. *Toxicol Lett*. 2009; 184: 18–25.
36. Gao S, Wu J, Liu R, et al. Interaction of NS2 with AIMP2 facilitates the switch from ubiquitination to SUMOylation of M1 in Influenza A virus-infected cells. *J Virol*. 2015; 89: 300–311.
37. Yang X, Jiang B, Song X, et al. Fast axial-scanning photoacoustic microscopy using tunable acoustic gradient lens. *Opt Express*. 2017; 25: 7349–7357.
38. Jiang B, Yang X, Luo Q. Reflection-mode Bessel-beam photoacoustic microscopy for in vivo imaging of cerebral capillaries. *Opt Express*. 2016; 24: 20167–20176.
39. Cui X, Zhang J, Du R, et al. HSF4 is involved in DNA damage repair through regulation of Rad51. *Biochim Biophys Acta*. 2012; 1822: 1308–1315.